

Multi-Objective Optimization of an Interior PM Motor for a High-Performance Drive

Nicola Bianchi, Dario Durello and Emanuele Fornasiero

Abstract—This paper shows the results of the optimization of an Interior Permanent Magnet (IPM) motor for a high performance drive. A multi-objective is considered in the optimization process, mainly considering two motor capabilities. The first objective is the maximization of the torque density of the motor. This means that the torque is maximized for given external dimension and for given current density (i.e., given electric loading). The second objective deals with the sensorless detection of the rotor position. A technique based on the high-frequency signal injection is considered. The IPM motor has to keep the capability to be sensorless detected when it works at any load. In particular, such a capability has to be verified along the trajectory of the Maximum Torque per Ampere (MTPA), that is, the rotor has to exhibit a proper differential saliency (typically not lower than two) along all the MTPA trajectory, including overload operating conditions.

Index Terms—AC motor drives, Finite Element analysis, Interior PM machines, Machine design, Optimization, Permanent-magnet machines, Synchronous machines, Variable-speed drives.

I. INTRODUCTION

THE Interior Permanent Magnet (IPM) motor [1] is becoming very attractive for high-performance motor drives [2], [3]. The IPM rotor is formed by several flux-barriers where the permanent magnets are inset. Such barriers also obstacle the flux lines along the direction of the PM flux, but not in the quadrature directions. Thus, the rotor becomes anisotropic.

Such a rotor structure gives peculiar capabilities to the IPM motor. Among the others, they are:

- The motor torque is due to two components: the PM torque that is proportional to the PM flux in the rotor, and the reluctance torque that is due to the rotor anisotropy [4]. This yields a higher degree of freedom in designing the machine: the proper combination of the two torque components allows the motor to operate in a wide constant power speed range.
- The rotor anisotropy can be employed so as to sensorless detect the rotor position, i.e., via a technique based on the high frequency signal injection [5], [6]. The different magnetic permeance along the direct and the quadrature axis of the rotor cause a modulation of the high-frequency signal injected which is related to the rotor position.

This paper is focused on the optimization by means of genetic algorithm (GA) of the IPM motor [7], [8]. A multi-objective optimization is carried out so as to maximize two motor capabilities.

- 1) The first objective is to maximize the torque. The IPM motor external dimension are fixed as well as the current density in the conductors (i.e., the Joule losses of the machine). Then, the rotor geometry is changed so as to maximize the output torque.
- 2) The second objective considers the sensorless detection of the rotor position. The differential (incremental) saliency of the rotor is maximized. Since the IPM motor is operated along the trajectory of the Maximum Torque per Ampere (MTPA), the rotor has to exhibit a proper differential saliency (typically not lower than two) along all the MTPA trajectory.

Details will be given in the next section.

II. FITNESS FUNCTION OPTIMIZATION

The IPM machine under optimization has a number of slots $Q = 48$ and a number of poles $2p = 4$. Fig. 1 shows the reference machine.

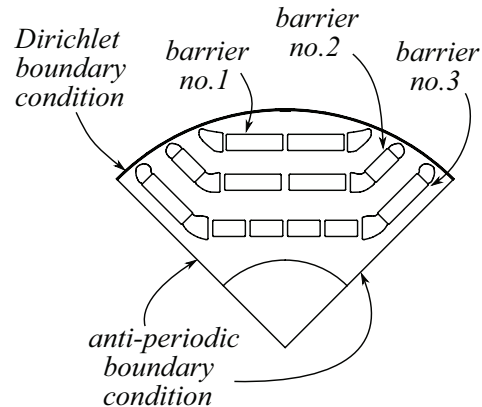


Fig. 1. Motor geometry used for the optimization.

The machine exhibits a magnetic periodicity, so that only a portion of the whole machine is analyzed. This is an advantage to reduce the finite elements analysis (FEA) simulation time. The machine is divided in $GCD(Q, 2p) = 4$ parts, thus only one fourth is simulated. Proper anti-periodic magnetic conditions are adopted on the boundary, as highlighted in Fig. 1.

The simulation process aims to determine the two optimization variables, the torque and the high frequency electromagnetic saliency. As it will be seen in the following, four FEA simulations are enough to determine the parameters for built the optimization fitness function.

A. Torque determination

The MTPA trajectory is defined as the trajectory of the current vector along which the ratio between the torque and the corresponding current vector amplitude is maximized. In

Nicola Bianchi, Dario Durello and Emanuele Fornasiero are with the Department of Industrial Engineering, University of Padova, via Gradenigo 6/A, 35131 Padova (ITALY) (e-mail: nicola.bianchi@dii.unipd.it, dario.durello@unipd.it, emanuele.fornasiero@unipd.it).

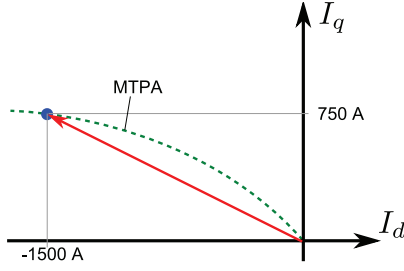


Fig. 2. Nominal current working point.

IPM motors, such trajectory stands on the second quadrant of the dq plane, see Fig. 2.

The working point for the torque determination is selected with the motor supplied by the nominal current, on the MTPA trajectory. The nominal current amplitude is related to a current density equal to $J = 9.5 \text{ A/mm}^2$, chosen on the base of thermal considerations.

During the optimization of the machine, the phase of the current vector can change, since the MTPA trajectory is modified. Anyway the same working point is adopted for all the machines, even if it is an approximation. For the torque determination, this is precautionary. The nominal torque T_n is determined in the first FEA simulation. From the same field solution, the nominal d - and q -axis flux linkages, $\lambda_{d,n}$ and $\lambda_{q,n}$ are computed.

B. Saliency determination

According to the injection of a HF rotating voltage, the current vector trajectory in the dq plane results as represented in Fig. 3.

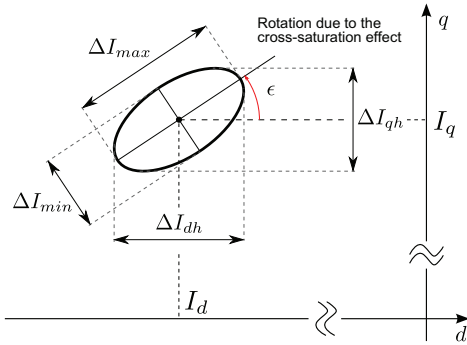


Fig. 3. HF current vector trajectory.

The HF current in the dq plane is an ellipse. The length of the major axis represents the maximum amplitude of the HF current variation (ΔI_{max}), while the minor axis represents its minimum amplitude (ΔI_{min}). The ratio between the maximum and the minimum HF current variation determines the HF saliency ξ_{HF} :

$$\xi_{HF} = \frac{\Delta I_{max}}{\Delta I_{min}} \quad (1)$$

The ellipse axes are not parallel to the dq axes. The displacement angle ϵ is due to the effect of the cross-saturation, i.e. to the presence of the mutual differential inductance $L_{dq} = L_{qd}$.

The current ellipse can be considered as the sum of two rotating vectors in opposite directions, a backward and a forward rotating vector [9]. The major ellipse axis is

determined by the sum of the amplitude of the backward and the forward rotating current vectors, while the minor axis is determined by their difference. The saliency ξ_{HF} is then equal to the ratio between their sum and their difference. Expressing the currents as a function of the d -axis and q -axis differential inductances, L_d and L_q and of the mutual differential inductances, $L_{dq} = L_{qd}$ (remember that $L_{dq} = L_{qd}$ for the principle of conservation of energy), the HF saliency results in:

$$\xi_{HF} = \frac{(L_d + L_q) + \sqrt{(L_d - L_q)^2 + 4L_{dq}^2}}{(L_d + L_q) - \sqrt{(L_d - L_q)^2 + 4L_{dq}^2}} \quad (2)$$

For the determination of the HF saliency, the differential inductance model has to be determined:

$$\mathbf{L} = \begin{bmatrix} L_d & L_{dq} \\ L_{qd} & L_q \end{bmatrix} \quad (3)$$

The matrix \mathbf{L} is used to determine the d -axis and q -axis HF currents consequent to the injection of HF voltages. From the HF voltage, the HF flux linkages can be determined by:

$$\begin{bmatrix} \lambda_d \\ \lambda_q \end{bmatrix} = \begin{bmatrix} L_d & L_{dq} \\ L_{qd} & L_q \end{bmatrix} \begin{bmatrix} i_d \\ i_q \end{bmatrix} \quad (4)$$

The currents are determined from:

$$\begin{bmatrix} i_d \\ i_q \end{bmatrix} = \mathbf{L}^{-1} \begin{bmatrix} \lambda_d \\ \lambda_q \end{bmatrix} \quad (5)$$

where \mathbf{L}^{-1} is the inverse matrix of \mathbf{L} .

It is a small signal model that is computed around the operating point. It should require four additional FEA simulations, as can be seen in Fig. 4.

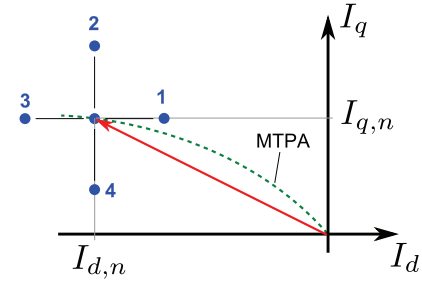


Fig. 4. Four simulations to determine the small-signal inductance model.

In order to reduce the computation time, only two additional simulations are carried out, Fig. 5. To determine the derivative of the flux linkages with respect to the variation of the d -axes currents, i.e. $\partial \lambda_d / \partial i_d$ and $\partial \lambda_q / \partial i_d$, the first of the two simulations is carried out with the same current on the q -axis, but with an increased current on the d -axis, ΔI_d . Such derivatives are approximated by:

$$L_d = \frac{\partial \lambda_d}{\partial i_d} \simeq \frac{\lambda_{d,\Delta I_d} - \lambda_{d,n}}{\Delta I_d} \quad (6)$$

and

$$L_{qd} = \frac{\partial \lambda_q}{\partial i_d} \simeq \frac{\lambda_{q,\Delta I_d} - \lambda_{q,n}}{\Delta I_d} \quad (7)$$

where $\lambda_{d,\Delta I_d}$ and $\lambda_{q,\Delta I_d}$ are the flux linkages derived from this simulation and $\lambda_{d,n}$ and $\lambda_{q,n}$ are the flux linkages derived from the first simulation.

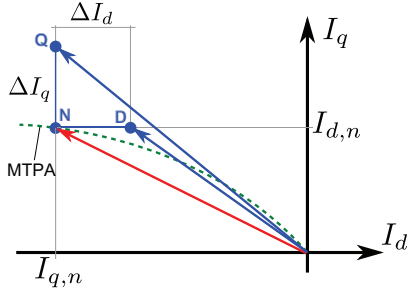


Fig. 5. Two FEA simulations to determine the small-signal inductance model

The second simulation is carried out with the same current on the d -axis, but with an increased current on the q -axis, ΔI_q . In this case, the derivatives of the flux linkages with respect to the q -axis current are determined, i.e. $\partial \lambda_d / \partial i_q$ and $\partial \lambda_q / \partial i_q$. With the same approximation of the previous case, they are:

$$L_{dq} = \frac{\partial \lambda_d}{\partial i_q} \simeq \frac{\lambda_{d,\Delta I_q} - \lambda_{d,n}}{\Delta I_q} \quad (8)$$

and

$$L_q = \frac{\partial \lambda_q}{\partial i_q} \simeq \frac{\lambda_{q,\Delta I_q} - \lambda_{q,n}}{\Delta I_q} \quad (9)$$

where $\lambda_{d,\Delta I_q}$ and $\lambda_{q,\Delta I_q}$ are the flux linkages derived from this simulation.

C. Demagnetization

One effect of the stator current reaction is to decrease the flux-density of the magnet, approaching the knee of the B-H curve. A minimum value of the PM flux density is fixed as a limit, so as to avoid the irreversible demagnetization of the permanent magnets. Hence, a third and last simulation is carried out with only negative d -axis current, with amplitude equal to the nominal current. The aim is to check the PM demagnetization level, in order to avoid the selection of solutions that exhibit demagnetization problems. In such cases, the corresponding solution is not considered.

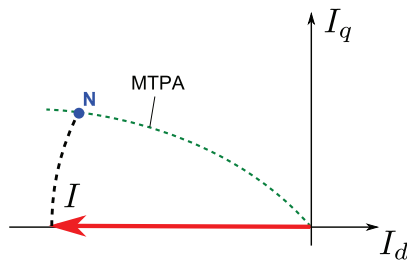


Fig. 6. Simulation to check the PM demagnetization

III. OPTIMIZATION CONSTRAINTS

The design procedure focuses on an IPM motor for traction application. The main data are summarized in Table I.

The constraints in the design are split in geometrical limits and operating limits.

A. Geometrical constraints

The first constraint that is considered is the maximum external diameter. It has been fixed equal to $D_e = 460$ mm. The length of the motor is fixed equal to $L_{stk} = 500$ mm.

A further constraint deals with the air gap thickness, that is fixed to be equal to $g = 1$ mm.

TABLE I
MAIN MOTOR DATA

| Variable | symbol | measure | unity |
|-----------------------------|--------|---------|-------|
| Number of slots | 48 | – | |
| Number of poles | 4 | – | |
| External diameter D_e | 460 | (mm) | |
| Air-gap diameter D_i | 298 | (mm) | |
| Active length L_{stk} | 500 | (mm) | |
| End winding length L_{ew} | 300 | (mm) | |
| PM coercive field | 726 | (kA/m) | |
| PM recoil permeance μ_r | 1.04 | – | |

B. Operating limit constraints

There are two limits that have been fixed in the design.

The first limit deals with the maximum losses of the motor. They are linked to the capability to dissipate the heat via the external surface of the motor frame.

The second limit deals with the demagnetization of the PMs, that has been fixed equal to $B_{min} = 0.4$ T, considering NdFeB magnets at high temperature.

IV. DESIGN VARIABLES

The rotor geometry is chosen to be optimized. It is formed by three flux-barriers per pole. Table II reports the design variables.

TABLE II
DESIGN VARIABLES.

| Variable | symbol | measure | unity | range |
|------------------------|------------|---------|-------|---------|
| PM thickness | t_m | mm | | 8 12 |
| PM widths | w_{m1} | mm | | 30 33 |
| | w_{m2} | mm | | 35 40 |
| | w_{m3} | mm | | 13 20 |
| | w_{m2l} | mm | | 18 22 |
| | w_{m3l} | mm | | 26 34 |
| distances from center | D_{m1} | mm | | 255 268 |
| | D_{m2} | mm | | 204 218 |
| | D_{m3} | mm | | 148 160 |
| | D_{m2l} | mm | | 256 268 |
| | D_{m3l} | mm | | 245 251 |
| angles of barrier ends | α_1 | deg | | 40 45 |
| | α_2 | deg | | 52 57 |
| | α_3 | deg | | 74 77 |

Several geometrical variables are changed during the optimization process. They refers to the dimensions shown in Figs. 7.

The PM thickness is kept constant for all the flux-barrier. Then the PM widths, the angles of barrier ends, and the distance from center are optimized for each barrier.

V. OPTIMIZATION PROCESS

The aim of the optimization is to maximize both the nominal torque T_{em} and the high frequency saliency ξ_{HF} . The optimization is carried out by means of weighted-sum method [10], in which the optimization is carried-out assigning a weight w_i to each objective z_i . Therefore the fitness function fit is evaluated as:

$$fit = \sum_{i=1}^N w_i z_i \quad (10)$$

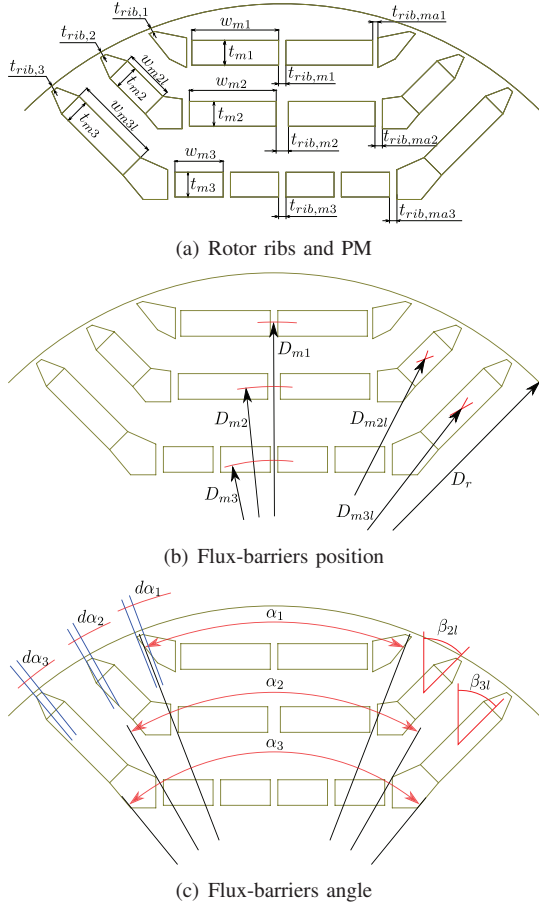


Fig. 7. Rotor geometry variables

where N is the number of objectives to optimize. The main advantage of these method is that a single objective optimization can be used [11].

The interface between the machine model and the genetic algorithms is highlighted in Fig. 8. The optimization procedure operates as follows. In the first generation, design

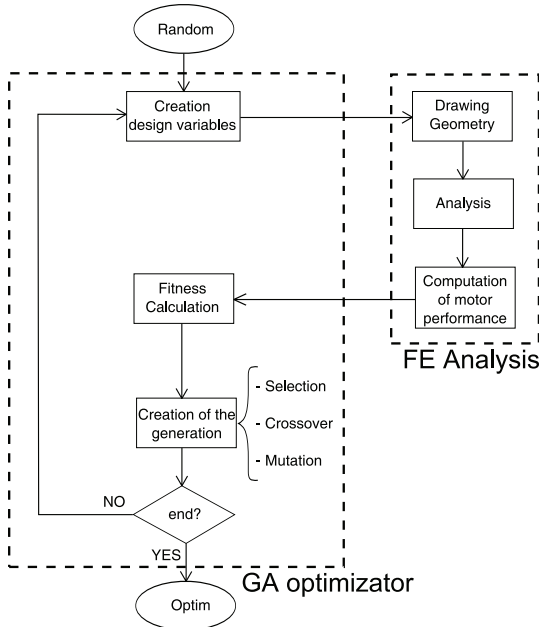


Fig. 8. Structure of the genetic algorithm

variables (the population) are selected randomly, into the range values reported in Table II. When the first generation

is fully defined and analysed, a new generation is created. The **natural selection** is achieved replacing the elements (the motors) with worst fitness with the offspring created from the **crossover** of the best elements of the population. The choice of such elements is carried out by means of the method of the roulette wheel rank [11]. In order to increase the search region, a probability of **mutation** p_{mut} is also included. A FEA of the motor is linked with the optimizer. The IPM motor structure is drawn automatically. The computation of the output results is carried-out as described in Section II. Finally, the GA optimizer reads the output results. From the torque and high frequency saliency, the **fitness function** is calculated evaluating the two objectives $\frac{\xi_{HF}}{\xi_{REF}}$ and $\frac{T_{em}}{T_{REF}}$. The coefficients T_{REF} and ξ_{REF} are chosen in order to normalize both torque and saliency. Whether a machine is demagnetized, the objective function is imposed equal to zero. The algorithm ends to run when the number of generations N_{gen} is reached.

VI. RESULTS OF THE OPTIMIZATION PROCESS

The parameters of GA optimization are shown in Table III. The results are presented hereafter. Fig. 9 shows the trends of the best and average fitness in the population, with the GA parameter of Table III as a function of the generation number. When the number of generations increases, the fitness of the individuals improve close to the best of the generations fitness value. Fig. 10 shows the design variables versus the number of generations. From the first to the last generations, some variables tends to assume values in a limited range (e.g. angle of the first barrier, magnet thickness). This means that an optimal value exist for such a variable. Hence these variables have great impact on the optimization objective.

Conversely, other variables cover a wide range of value in each generation (e.g. First barrier and second lateral barrier PM width). This means that their impact in the optimization objectives is low.

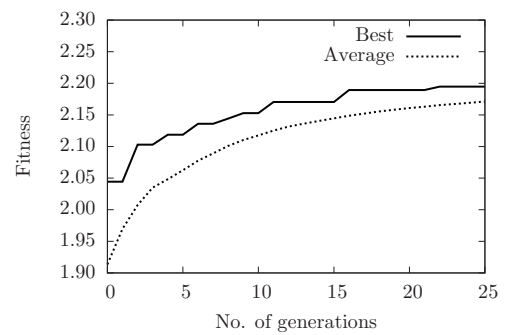


Fig. 9. Average and best fitness trend during the optimization

TABLE III
LIST OF THE PARAMETER TO INITIALIZE THE GENETIC ALGORITHM

| | Symbol | Value |
|-----------------------------|-------------|-------|
| Number of bits per variable | N_{bit} | 8 |
| Population size | N_{pop} | 200 |
| Number of generations | N_{gen} | 25 |
| Probability of mutation | p_{mut} | 0.03 |
| Probability of crossover | p_{cross} | 0.70 |

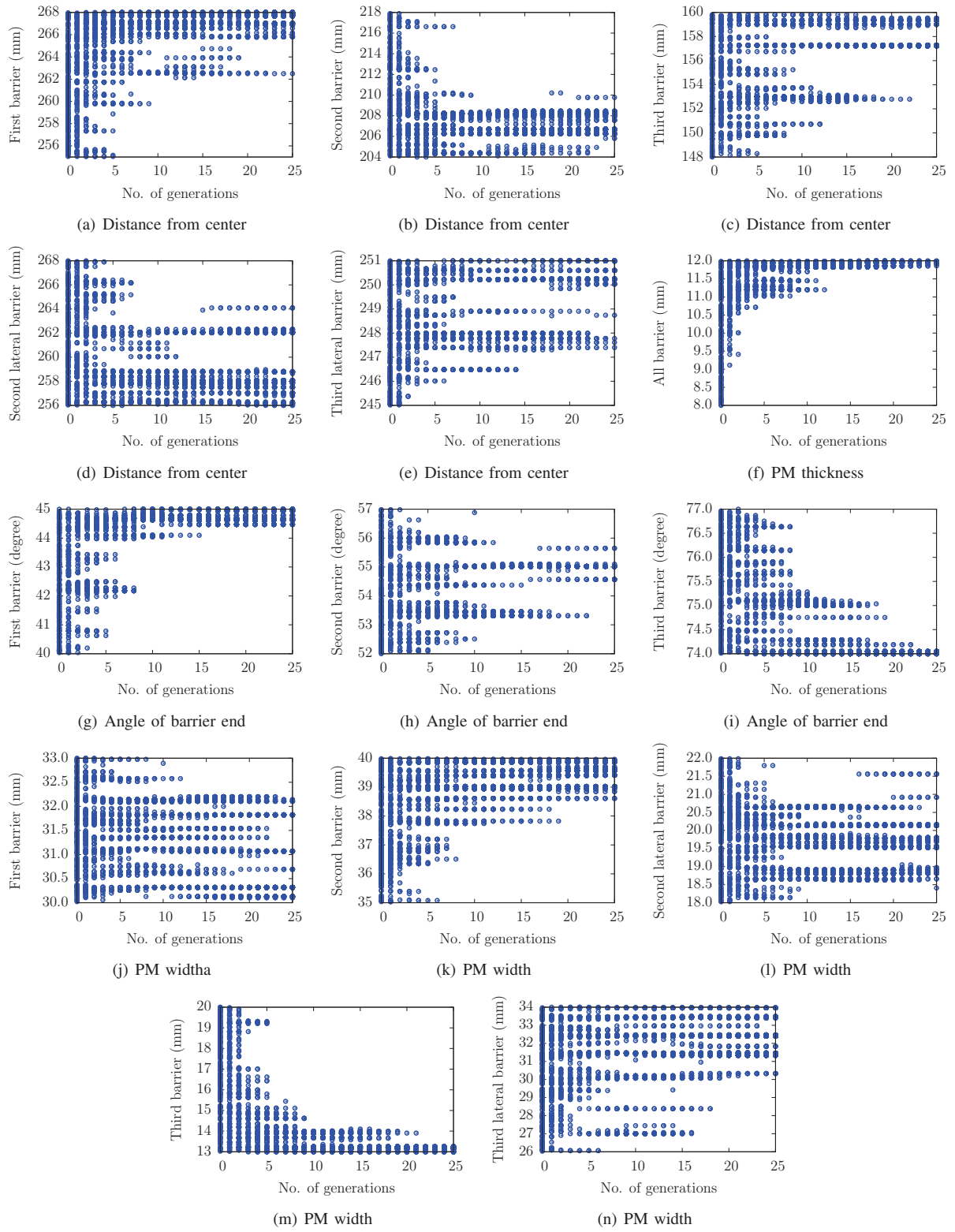


Fig. 10. Distribution of the population during the optimization process

As regards the behavior of the design variables during the optimization process:

- The first and third barriers move toward the air gap.
- The effects of the second and third lateral barriers are negligible (in the optimization process).
- The magnet thickness tends to increase.
- The angle span of first barrier increases while the angle span of the third barrier tends to decrease. The second barrier width has low effect.
- Finally the magnet width has low influence in the fitness function computation. Only the third barrier width requests low value.

In Fig. 11 all the outputs obtained during the optimization process are reported in the objective plane Torque–Saliency, using grey dots. In particular the white points show the best machines of each generation (i.e. with maximum fitness) obtained during the optimization process. It is worth noticing that the optimization of the rated torque is opposite to the optimization of the HF saliency. When the torque increases, IPM motor solutions with higher HF saliency yields a slight decrease of the average torque or vice versa. It can be noted that optimization of torque and HF saliency has an opposite trend.

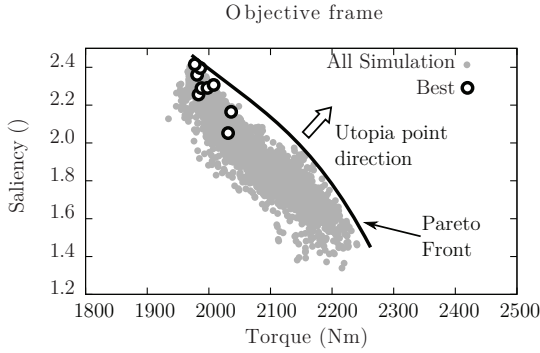


Fig. 11. Objective values of the machines analysed in the optimization process

Choosing a single fitness function (which includes HF saliency and average torque), a multi-objective optimization is reduced to a single-objective optimization. Therefore, the machines with the maximum fitness move along the Pareto front in the direction of higher saliency and lower torque or vice versa.

The differences between the rotors of the initial and of the optimal machine are compared in Table IV. It reports both the design variables and the objective outputs. It is worth noticing that the initial machine can be considered a good designed. In fact, in the objective plane Torque–Saliency of Fig. 11, it is located near the Pareto front. Anyway, the fitness of the optimized machine is almost 10% better than the initial machines, due to a HF saliency increases of about 40% and a torque decrease of about 12%.

The last element of Table IV shows the magnet volume of the two machines. Even though the cost of the machine material is not implemented as penalty of the fitness function, the magnet quantity of the two machines remains almost the same.

Fig. 12 compares graphically the initial machine (a) and the optimal machine (b). The optimal machine exhibits some of the features of Fig. 10 as third barrier magnet width lesser than the reference one, the increasing magnet thickness and

TABLE IV
INPUT AND OUTPUT VALUES FOR THE STARTING AND OPTIMAL MACHINE

| machine | INITIAL | OPTIMAL |
|--------------------------|---------|---------|
| t_m [mm] | 10.15 | 11.97 |
| w_{m1} [mm] | 35.5 | 30.13 |
| w_{m2} [mm] | 35.5 | 39.57 |
| w_{m3} [mm] | 19.7 | 13.22 |
| w_{m2l} [mm] | 20.5 | 19.55 |
| w_{m3l} [mm] | 35.5 | 31.33 |
| D_{m1} [mm] | 257.85 | 268 |
| D_{m2} [mm] | 207.8 | 206.69 |
| D_{m3} [mm] | 149.84 | 157.27 |
| D_{m2l} [mm] | 258.7 | 257.51 |
| D_{m3l} [mm] | 241 | 250.25 |
| α_1 [deg] | 42.46 | 44.63 |
| α_2 [deg] | 55 | 55.02 |
| α_3 [deg] | 76 | 74.05 |
| T_{em} [Nm] | 2227 | 1978 |
| ξ_{HF} | 1.69 | 2.34 |
| fitness | 1.96 | 2.16 |
| Magnet Volume [dm^3] | 1.35 | 1.41 |

different barrier position. The loss of barrier regularity is due to the automatic geometric drawing and a possible regularized structure can be carried out.

Hence the rotor geometry of Fig. 12 (b) is modified as shown in Fig. 12 (c). As shown in Table V, the barrier regularization yields an increasing of the torque to 1993 Nm but a decrease of HF Saliency down to 2.22.

TABLE V
OBJECTIVES VALUES OPTIMIZE MACHINE VERSUS REGULARIZED MACHINE

| machine | T_{em} [Nm] | ξ_{HF} |
|-----------------|---------------|------------|
| First Optimal | 1978 | 2.34 |
| Regular barrier | 1993 | 2.22 |

The optimized machine has been studied by means of FEA, computing the saliency and the torque in the dq current plane. They are represented in Fig. 13, together with the current vector that has been used during the optimization process. Since during the optimization the machine geometry is changed, the current vector is no more on the MTPA trajectory. However, the optimization algorithm found the optimum torque and saliency for such current vector. As represented in Fig. 13, moving the current vector toward the d -axis, the saliency ξ increases while the torque decreases, while moving the current vector toward the q -axis the torque increases and the saliency decreases. Hence, during the optimization process, the MTPA curve of the machine moves toward the q -axis, since the region with higher saliency is below such curve.

VII. CONCLUSIONS

This paper focuses on the optimization of IPM motor considering the average torque and the HF saliency (i.e. the capability to sensorless detect the rotor position) as the objectives of the optimization. Both geometrical limits and the PM demagnetization are considered as constraints in the optimization process.

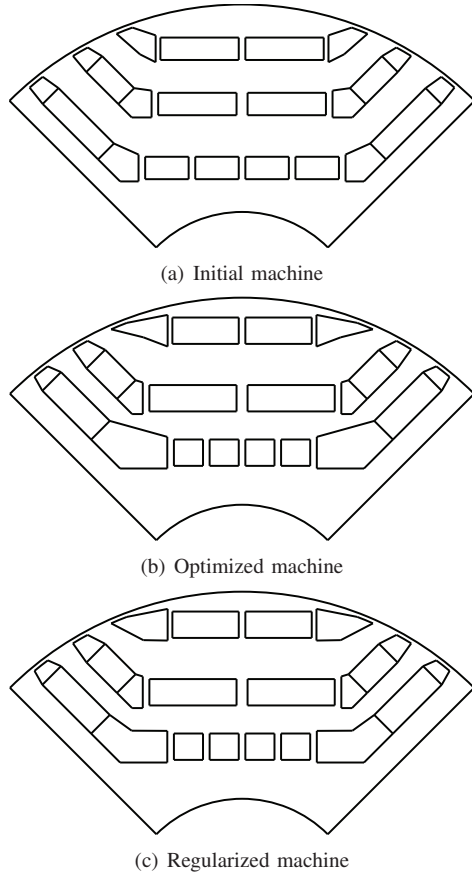


Fig. 12. Rotor geometry for the initial machine (a), the optimize machine (b) and the regularized machine (c)

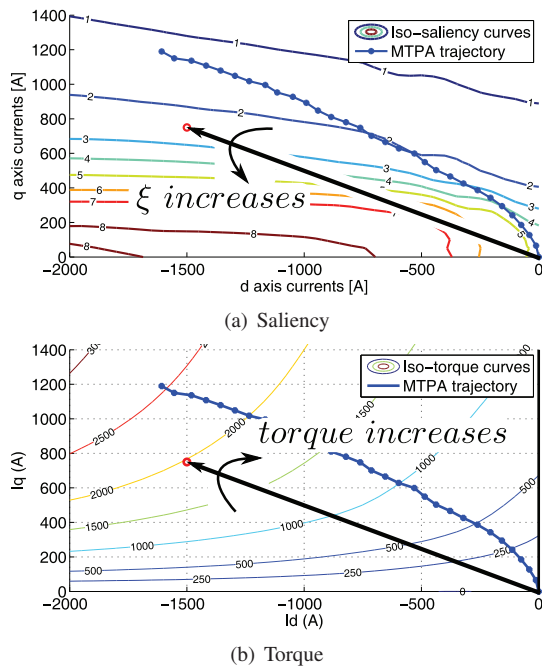


Fig. 13. Saliency and torque on the dq plane

The result achieved shows that the two objectives are in opposition, so that the optimal machine is able to exhibit higher HF saliency to the disadvantage of a lower average torque and vice versa. The HF saliency tends to increase when the rotor barriers lose regularity. Whether the regularity is held, the torque can be increased with an acceptable HF saliency.

REFERENCES

- [1] N. Bianchi and T. Jahns (editors), *Design, Analysis, and Control of Interior PM Synchronous Machines*, ser. IEEE IAS Tutorial Course notes, IAS'04 Annual Meeting. Seattle: CLEUP, Padova (Italy), October 3 2004, (info@cleup.it).
- [2] G. Foo and M. Rahman, "Sensorless Sliding-Mode MTPA Control of an IPM Synchronous Motor Drive Using a Sliding-Mode Observer and HF Signal Injection," *IEEE Transactions on Industrial Electronics*, vol. 57, no. 4, pp. 1270–1278, April 2010.
- [3] M. Haque and M. Rahman, "Incorporating control trajectories with the direct torque control scheme of interior permanent magnet synchronous motor drive," *Electric Power Applications, IET*, vol. 3, no. 2, pp. 93–101, March 2009.
- [4] E. Armando, P. Guglielmi, G. Pellegrino, M. Pastorelli, and A. Vagati, "Accurate modeling and performance analysis of IPM-PMASR motors," *IEEE Transactions on Industry Applications*, vol. 45, no. 1, pp. 123–130, Jan.-feb. 2009.
- [5] H. D. Kock, M. Kamper, and R. Kennel, "Anisotropy Comparison of Reluctance and PM Synchronous Machines for Position Sensorless Control Using HF Carrier Injection," *IEEE Transactions on Power Electronics*, vol. 24, no. 8, pp. 1905–1913, August 2009.
- [6] S. Bolognani, S. Calligaro, R. Petrella, and M. Tursini, "Sensorless Control of IPM Motors in the Low-Speed Range and at Standstill by HF Injection and DFT Processing," *IEEE Transactions on Industry Applications*, vol. 47, no. 1, pp. 96–104, Jan.-Feb. 2011.
- [7] G. Pellegrino and F. Cupertino, "IPM motor rotor design by means of FEA-based multi-objective optimization," in *2010 IEEE International Symposium on Industrial Electronics (ISIE)*, July 2010, pp. 1340 – 1346.
- [8] K.-J. Han, H.-S. Cho, D.-H. Cho, and H.-K. Jung, "Optimal core shape design for cogging torque reduction of brushless DC motor using genetic algorithm," *IEEE Transactions on Magnetics*, vol. 36, no. 4, pp. 1927 –1931, July 2000.
- [9] P. Guglielmi, M. Pastorelli, and A. Vagati, "Cross-Saturation Effects in IPM Motors and Related Impact on Sensorless Control," *IEEE Transactions on Industry Applications*, vol. 42, no. 6, pp. 1516 –1522, nov.-dec. 2006.
- [10] A. Konak, D. W. Coit, and A. E. Smith, "Multi-objective optimization using genetic algorithms: A tutorial," *Reliability Engineering & System Safety*, vol. 91, no. 9, pp. 992 – 1007, 2006, special Issue - Genetic Algorithms and Reliability.
- [11] R. L. Haupt and S. E. Haupt, *PRACTICAL GENETIC ALGORITHMS*, ser. Wiley-interscience. John Wiley & Sons, Inc., Hoboken, New Jersey., 2004.

VIII. BIOGRAPHIES

Nicola Bianchi (SM'09) received the Laurea and Ph.D. degree in Electrical Engineering at University of Padova, Padova Italy, in 1991 and 1995 respectively. Since 2005 he was an Associate Professor in Electrical Machines, Converters and Drives, at the Electric Drive Laboratory, Department of Industrial Engineering, of the University of Padova. He is author and co-author of several scientific papers on electrical machines and drives.

Dario Durello received the B.S. degree in Automation Engineering and the M.S. degree in Electrical Engineering from the University of Padova, Italy, in 2006 and 2010 respectively. Since 2010 he has been working in the Electric Drives Laboratory of the Department of Electrical Engineering. His research activities are concentrated on the design and optimization of permanent magnet synchronous machines.

Emanuele Fornasiero received the Laurea degree in Electrical Engineering and the PhD degree from the University of Padova, in 2006 and 2010, respectively. During the PhD he was involved in the analysis of rotor losses in fractional slot PM machines and in fault tolerant applications. Now he is a research assistant at University of Padova, and his activity deals with the design of PM machines.